AGU PUBLICATIONS

JGR

Journal of Geophysical Research: Earth Surface

RESEARCH ARTICLE

10.1002/2016JF003903

Key Points:
- We document a 5 times/1–2\Psi decrease in bed thickness/grain size with 20 m elevation change above the thalweg of a submarine channel
- Rapid facies change in coeval deposits from the channel axis to margin requires a change in elevation above the submarine channel thalweg
- Numerical model reproduces grain-size and bed thickness trends, enabling facies prediction in similar channelized architectures

Supporting Information:
- Supporting Information S1
- Figure S1
- Table S1
- Table S2
- Table S3
- Table S4

Correspondence to:
Z. Jobe,
zanejobe@gmail.com

Citation:
Jobe, Z., Z. Sylvester, M. B. Pittaluga, A. Frascati, C. Pirmez, D. Minisini, N. Howes, and A. Cantelli (2017), Facies architecture of submarine channel deposits on the western Niger Delta slope: Implications for grain-size and density stratification in turbidity currents, *J. Geophys. Res. Earth Surf.*, *122*, doi:10.1002/2016JF003903.

Received 28 MAR 2016
Accepted 14 JAN 2017
Accepted article online 25 JAN 2017

©2017. American Geophysical Union. All Rights Reserved.

Facies architecture of submarine channel deposits on the western Niger Delta slope: Implications for grain-size and density stratification in turbidity currents

Zane Jobe[1,2], Zoltán Sylvester[2,3], Michele Bolla Pittaluga[2], Alessandro Frascati[2], Carlos Pirmez[4], Daniel Minisini[2], Nick Howes[2], and Alessandro Cantelli[5]

[1]Department of Geology and Geological Engineering, Colorado School of Mines, Golden, Colorado, USA, [2]Clastics Research Team, Shell International Exploration and Production, Houston, Texas, USA, [3]Now at Clastic Stratigraphy Team, Chevron Energy Technology Company, Houston, Texas, USA, [4]Shell Italia Exploration and Production, Rome, Italy, [5]Shell Exploration and Production Company, Houston, Texas, USA

Abstract High-resolution bathymetry, seismic reflection, and piston core data from a submarine channel on the western Niger Delta slope demonstrate that thick, coarse-grained, amalgamated sands in the channel thalweg/axis transition to thin, fine-grained, bedded sands and muds in the channel margin. Radiocarbon ages indicate that axis and margin deposits are coeval. Core data show that bed thickness, grain size, and deposition rate strongly decrease with increasing height above channel thalweg and/or distance from channel centerline. A 5 times decrease in bed thickness and 1–2 ψ decrease in grain size are evident over a 20 m elevation change (approximately the elevation difference between axis and margin). A simplified in-channel sedimentation model that solves vertical concentration and velocity profiles of turbidity currents accurately reproduces the vertical trends in grain size and bed thickness shown in the core data set. The close match between data and model suggests that the vertical distribution of grain size and bed thickness shown in this study is widely applicable and can be used to predict grain size and facies variation in data-poor areas (e.g., subsurface cores). This study emphasizes that facies models for submarine channel deposits should recognize that grain-size and thickness trends within contemporaneous axis-margin packages require a change in elevation above the thalweg. The transition from thick-bedded, amalgamated, coarser-grained sands to thin-bedded, nonamalgamated, finer-grained successions is primarily a reflection of a change in elevation. Even a relatively small elevation change (e.g., 1 m) is enough to result in a significant change in grain size, bed thickness, and facies.

1. Introduction

Density stratification, the vertical change in sediment concentration, in turbidity currents is predicted by numerical models [*Felix*, 2002; *Cantero et al.*, 2009; *Abd El-Gawad et al.*, 2012; *Bolla Pittaluga and Imran*, 2014] and has been measured in flume experiments [*Garcia*, 1990; *Altinakar et al.*, 1996; *McCaffrey et al.*, 2003; *Felix et al.*, 2005; *Hosseini et al.*, 2006; *Straub et al.*, 2008, 2011; *Sequeiros et al.*, 2009, 2010; *Tilston et al.*, 2015]. Data from full-scale natural flows in submarine channels, however, are limited to velocity profiles [e.g., *Xu*, 2010], and *Talling et al.* [2015] state that a key future research direction is the direct measurement of density stratification in natural turbidity currents.

In outcrop exposures, channel margin thin-bedded facies are usually vertically offset from time-equivalent thick-bedded and coarser-grained channel axis strata [e.g., *Chapin and Keller*, 2007; *Kane and Hodgson*, 2011; *Khan and Arnott*, 2011; *Hubbard et al.*, 2014]. This pronounced facies change is the product of the density stratification within the flow (i.e., the upward decrease in sediment concentration and grain size [*Straub and Mohrig*, 2008; *Bolla Pittaluga and Imran*, 2014]). A number of studies interpret flow stratification from outcrop data [*Arnott*, 2007; *Dykstra and Kneller*, 2009; *Hubbard et al.*, 2014; *Hansen et al.*, 2015]. Some facies models for submarine channels incorporate these results [e.g., *Kane et al.*, 2010; *Hansen et al.*, 2015], but there is a persistence of facies models that assume quasi-horizontal fill and rapid lateral facies changes without appreciable difference in elevation between axis and margin deposits [e.g., *Campion et al.*, 2005; *McHargue et al.*, 2011].

Modern submarine channels are another valuable data source for interpreting density stratification because of the preserved geomorphology and the opportunity to sample recent stratigraphy. Sediment coring in

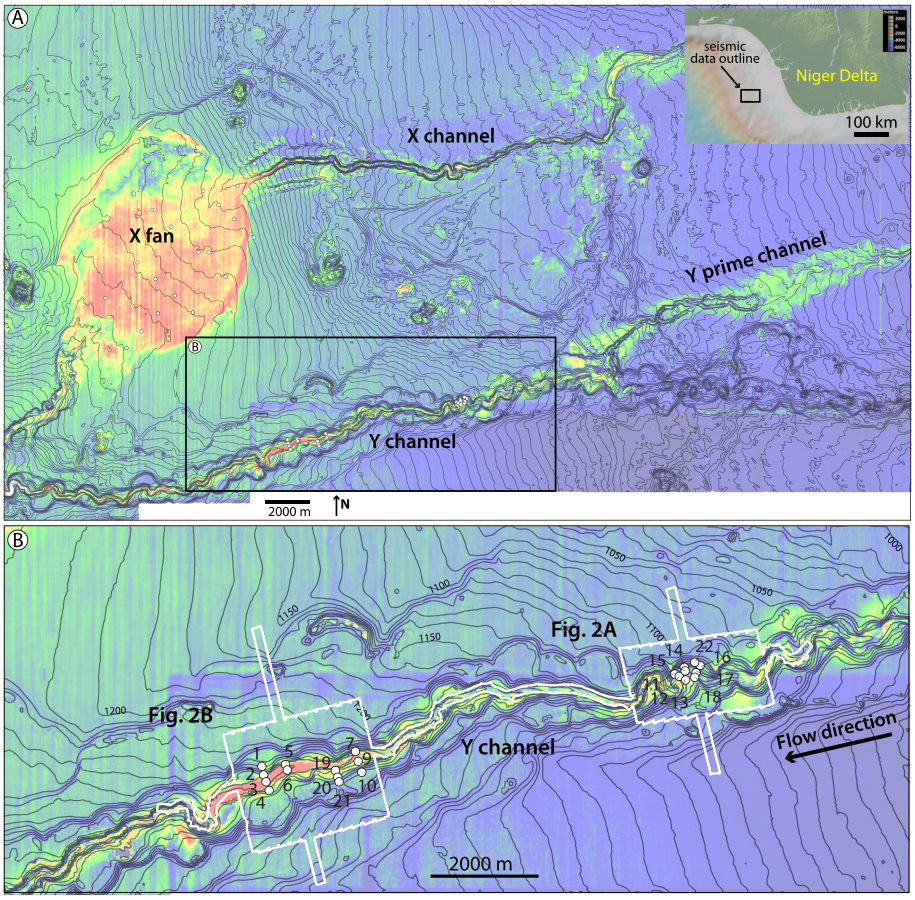

Figure 1. Map of the study area on the western Niger Delta slope. (a) Bathymetric map of the X, Y, and Y′ submarine channels; color is seafloor amplitude, and contours are seafloor bathymetry. High amplitudes (red colors) indicate sand deposition in and near the channels, while low amplitudes (blue colors) indicate muddy sediment. Piston core locations shown in white circles. (b) Detailed map of the Y channel system, with its abandoned (Y) and active (Y′) feeder channels. The white polygon denotes the location of the AUV multibeam bathymetry shown in Figure 2. Depth contours are in 10 m intervals.

modern submarine channels indicates that grain size and bed thickness decrease markedly with increasing height above the thalweg [*Hiscott et al.*, 1997; *Pirmez and Imran*, 2003; *Dennielou et al.*, 2006; *Babonneau et al.*, 2010; *Paull et al.*, 2010; *Kolla et al.*, 2012; *Migeon et al.*, 2012; *Jobe et al.*, 2015]. Some studies have linked these trends in bed thickness [*Dennielou et al.*, 2006] and grain size [*Migeon et al.*, 2012] to turbidity current flow properties, including concentration and velocity profiles.

This study uses a data set consisting of high-resolution subbottom seismic reflection profiles, sediment cores, and laser-derived grain-size distributions to describe and quantify lateral and vertical changes in facies, bed thickness, and grain size in submarine channels within a well-constrained geomorphologic and stratigraphic context [*Jobe et al.*, 2015]. We also apply a numerical model that solves vertical concentration and velocity profiles of turbidity currents flowing in a confined channel [*Bolla Pittaluga and Imran*, 2014] to the data set. The model reproduces the bed thickness and grain-size trends observed in the data set. We then explore the application of these results to facies prediction in data-poor areas, such as subsurface cores and poorly exposed outcrops.

2. Niger Delta Data Set

Pirmez et al. [2000] first studied this modern turbidite system, identifying three submarine channels, the X, Y, and Y-prime (Y′) channels (Figure 1). This study will focus on the geomorphology, stratigraphic architecture, and grain-size distribution of the modern Y channel (Figures 1 and 2); for more detailed discussion of the

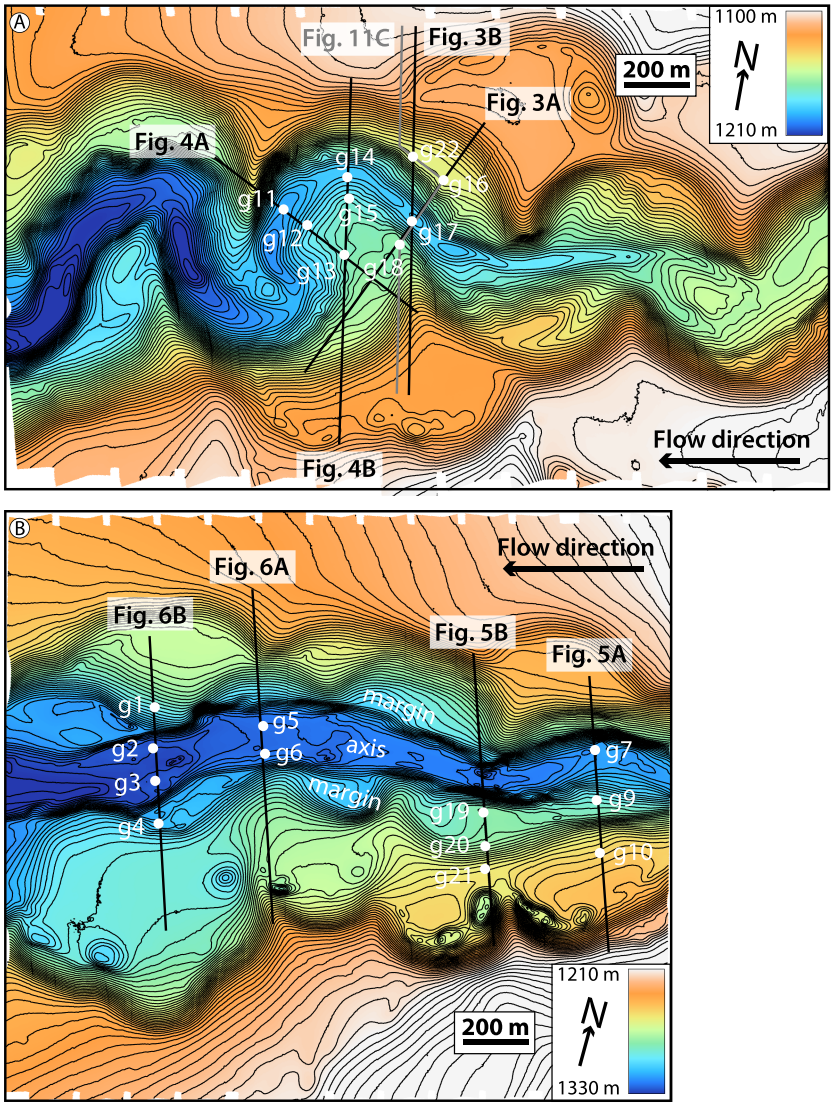

Figure 2. Bathymetry (1.5 m resolution) of the (a) upper and (b) lower portions of the Y channel. Note the locations of chirp subbottom profiles shown in Figures 3–6. The pronounced crescent-shaped terraces on the margins of the channel correspond to bends of an older, more sinuous channel. Piston core locations shown in white circles.

long-term evolution of the Y channel system, refer to *Jobe et al.* [2015] and *Parker et al.* [2016]. Three-dimensional seismic reflection data, twenty-one 10.16 cm diameter jumbo piston cores, and multibeam bathymetry and high-resolution 2-D subbottom profiles derived from an autonomous underwater vehicle (AUV) are used to characterize the study area (Figures 1 and 2). The AUV data were collected in 2012 and consist of (1) 12 km^2 multibeam bathymetry and backscatter data (gridded at 1.5 m) from a Kongsberg Simrad EM2040 300 kHz multibeam echo sounder (Figure 2) and (2) 124 line kilometer of very high resolution 2-D subbottom profiles from an Edgetech DW-106 chirp subbottom profiler operating at frequencies of 1–6 kHz (vertical resolution of ~0.2 m). Chirp profiles were converted from time to depth by using a water and sediment compressional velocity of 1500 and 1750 m/s, respectively (obtained from multisensor core logger data). The 21 jumbo piston cores were collected in 2007, and average core recovery was 10 m (Figure S1 in the supporting information). Cores were slabbed, logged with a Geotek multisensor core logger, photographed, X-rayed, and described at Texas A&M University. Core descriptions were digitized and tabulated in order to evaluate trends in bed thickness and grain size. We use the net-to-gross ratio (hereafter N:G), calculated from each core as the summed thickness of sand beds divided by the total "gross" thickness of the core. We exclude the hemipelagic drape in each core from the N:G

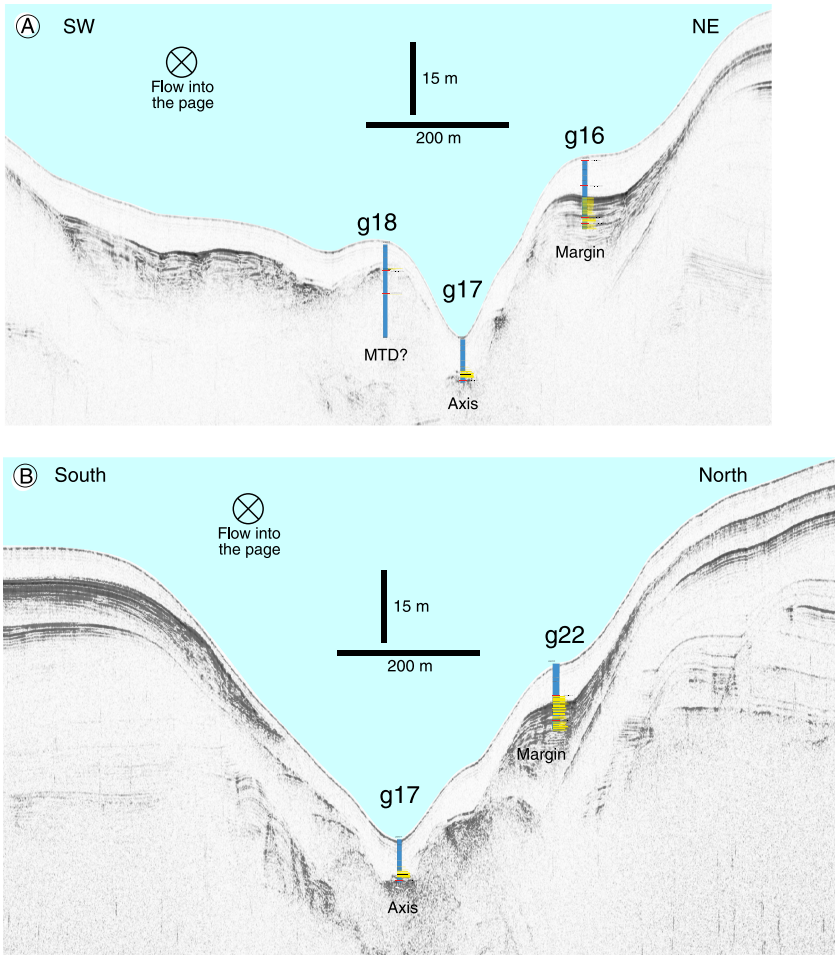

Figure 3. Chirp subbottom profiles of core transects (a) g16-g17-g18 and (b) g17-g22. Core descriptions overlain on chirp profiles. Margin deposits are thin-bedded and heterolithic (g16 and g22), while axis deposits are thick-bedded and amalgamated (g17). Core g18 penetrated a mass transport deposit on the margin of the channel. See Figure 2 for location of chirp profiles and cores.

calculation in order to more accurately delineate the lithology of the system when it was active. More than 400 grain-size samples from the cores were analyzed by using a Malvern Mastersizer 2000 particle-size analyzer (Table S1 in the supporting information). Samples for radiocarbon dating were prepared and analyzed according to details given in *Jobe et al*. [2015].

3. Facies Observations

Facies relationships within the Y channel are constrained by using chirp profiles and core data recovered from the margin and axis of the Y channel. The terminology "axis" and "margin" follow that of *Hubbard et al*. [2014] because the margin deposits onlap a previous erosional surface that confines the axis and margin (Figure 3); however, these margin deposits are not necessarily in physical continuity with sediments in the channel axis. These channel margin facies could also be classified as internal levee [*Kane and Hodgson*, 2011], inner levee [*Deptuck et al*., 2003, 2007; *Jobe et al*., 2015], or even overbank deposits; however, the data set suggests that these terms are not as mutually exclusive as a strict terminological approach would require. For further discussion of these terms and geometries, see *Kane and Hodgson* [2011] and *Hubbard et al*. [2014]. Sand beds in the Y channel exhibit features consistent with deposition by turbidity currents [*Bouma*, 1962; *Lowe*, 1982]. In the channel axis, thick, normally graded, structureless (e.g., S3/T_a division of *Lowe* [1982]) were deposited by high-density turbidity currents, where rapid sedimentation and turbulence damping [*Cantero et al*., 2011] suppress bed load movement. In the channel margin, thin-bedded,

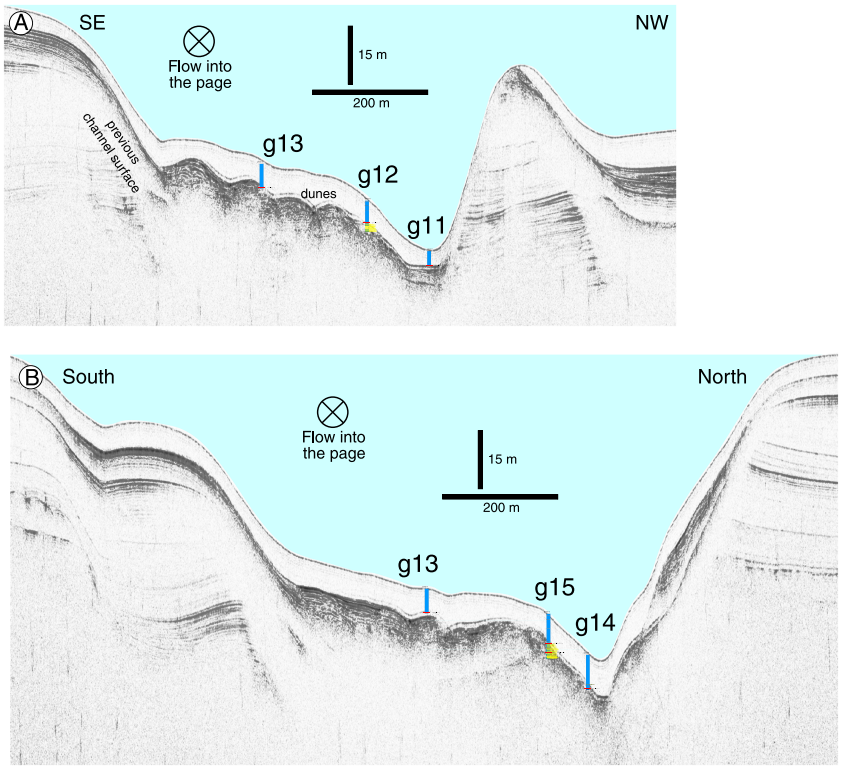

Figure 4. Chirp subbottom profiles of core transects (a) g11-g12-g13 and (b) g13-g14-g15 with overlain core descriptions. In Figure 4a, intrachannel dunes and a steep outer-bend channel bank are visible. These dunes are obscured by the Holocene mud drape and thus not visible on seafloor bathymetry. In Figure 4b, a wedge-shaped margin deposit on the northern margin of the channel thins against a previous channel surface. See Figure 2 for location of chirp profiles and cores.

structured (e.g., T_{bc} divisions of *Bouma* [1962]) sand beds were deposited by low-density turbidity currents [*Bouma*, 1962; *Lowe*, 1982]. The muddy interbeds consist of silt and clay, with moderate bioturbation. Few hybrid event beds are present in the study area [in the sense of *Lowe and Guy*, 2000; *Haughton et al.*, 2009]. Chirp profiles overlain with core data shown in Figures 3–6 demonstrate the facies relationships in the Y channel. Detailed core descriptions with grain-size distributions and radiocarbon dates are shown in Figures 7–11. At the seafloor, a clearly defined muddy unit (~4 m in thickness) visible in the chirp profiles is recovered by each core (Figures 3b and S1). This unit is almost exclusively clay and marks the abandonment of the Y channel at 19 ka [*Jobe et al.*, 2015]. The sand-rich deposits below this muddy unit represent active sand transport by turbidity currents during the Last Glacial Maximum from 25 to 19 ka (Figure 8) [*Jobe et al.*, 2015]. Radiocarbon ages from core data indicate that the axis (Figure 7) and margin (Figure 8) are contemporaneous. This indicates that the facies changes from axis to margin are due to vertical changes in the depositing flows.

Deposits in the channel axis consist of thick, amalgamated, structureless (i.e., T_a/S3 divisions) sand beds that commonly have mud rip-up clasts (cores g7 and g17 in Figure 7). Often, the piston coring apparatus penetrated these sand-rich deposits but was unable to recover them (cores g11 and g14 in Figure 4 and cores g2, g3, g5, and g6 in Figure 6) due to their consolidated and noncohesive nature. The chirp profiles show that the channel axis has few internal reflections (Figures 3–6), indicating a sandy, amalgamated environment. The channel axis locally contains mass-transport-deposits (MTDs), which are visible in both chirp profiles (Figure 3) and cores (g17 in Figure 7). The net-to-gross (N/G) of the channel axis is typically above 0.8, even with the presence of local MTDs. Grain-size analyses indicate a modal grain size of medium-grained sand, with the presence of grains larger than 2 mm (small gravel; Figure 7).

No reflections are traceable in the chirp profiles from the axis into the margin due to the presence of a steep slope (i.e., the channel bank) that separates the two facies (Figures 2 and 5). This surface is generally erosional

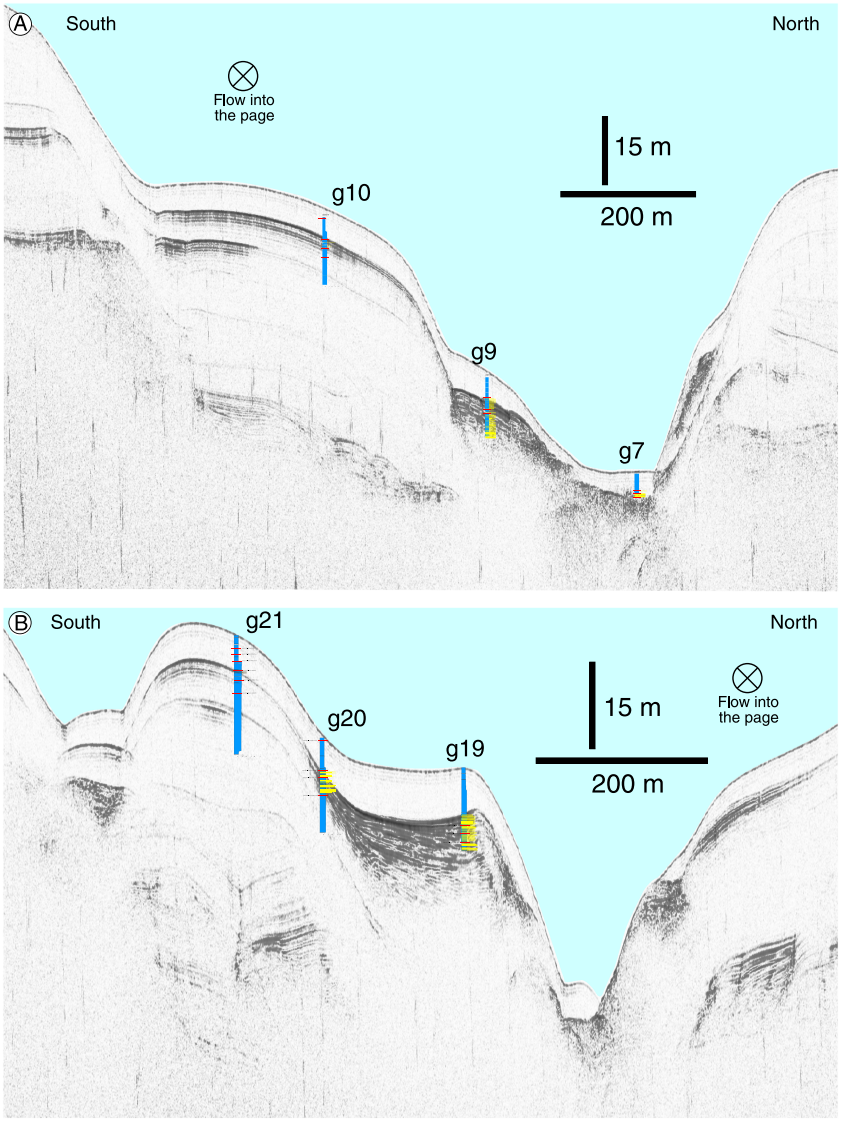

Figure 5. Chirp subbottom profiles of core transects (a) g7-g9-g10 and (b) g19-g20-g21 with overlain core descriptions. Both transects show dramatic thinning of the margin facies with increasing distance above and away from the channel thalweg. See Figure 2 for location of chirp profiles and cores.

in nature, with only a thin, muddy drape (e.g., Figure 5a). Margin deposits appear as lenses located adjacent to and 5–20 m above the thalweg/axis (Figures 3–6). In the margin of the Y channel, chirp profiles display continuous reflections of variable amplitude, indicating a more heterolithic and interbedded deposit (Figures 3–6). These reflections typically thin away from the channel and onlap against previous deposits (Figure 3a). In some cases, individual beds are mappable from proximal to distal margin and show dramatic thinning (Figure 5b). Core data demonstrate that the proximal margin, although not amalgamated, is very sand-rich, with N/G $>$ 0.6 (e.g., core g9 in Figure 5a). The medial and distal margins have more consistent bed thickness and lower N/G (Figure 10). A pronounced proximal to distal decrease in bed thickness, N/G, and deposition rate is clearly defined by multiple core transects (Figures 5, 6, and 10). For example, away from the channel, cores g19, g20, and g21 show decreases of N/G of 0.70, 0.24, and 0.03; mean sand bed thickness of 3.7, 1.3, and 0.8 cm, and deposition rate of 661.6, 80.7, 26.5 cm/ka (Figure 8, inset).

Many cores taken in the channel margin show a systematic decrease in sand bed thickness from core base to top, most prominently in core g4 (Figure 10). This trend has been attributed to progressive aggradation of the margin/levee [e.g., *Dennielou et al.*, 2006].

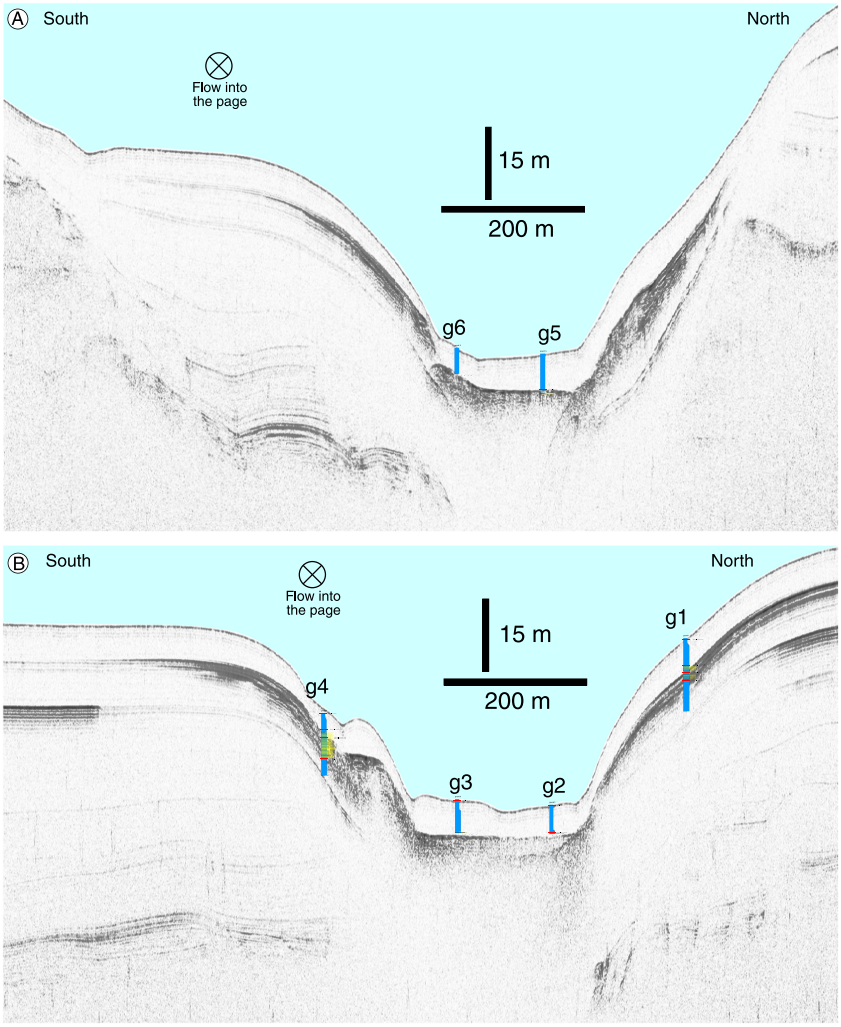

Figure 6. Chirp subbottom profiles of core transects (a) g5-g6 and (b) g1-g2-g3-g4 with overlain core descriptions. Poor recovery in the channel axis prevents full characterization, but chirp profiles suggests sandy, amalgamated facies. Margin facies consist of thin-bedded sand and mud interbeds (e.g., core g4), in a package thinning away from the channel axis. See Figure 2 for location of chirp profiles and cores.

Margin deposits are crescent shaped in planform (Figure 2) and wedge-shaped in cross section (Figure 5b). They are present on both the inner and outer banks of the Y channel (Figure 2), and typical dimensions are 200 m in the downstream direction, 100 m in the across-channel direction, and >10 m thick (Figures 3–6). Individual margin packages are isolated and disconnected from each other, either on opposite sides of the channel or, if on the same side, separated by geomorphic boundaries related to previous phases of channel migration (Figure 2) [see also *Jobe et al.*, 2015, Figures 6 and 14]. In areas of high sinuosity, the margin packages are preferentially deposited on the outer channel banks (Figure 2). The margin deposits are often asymmetric, with one side being thicker and more sand-rich (e.g., Figure 6b). The timing of emplacement of these margin packages is well constrained to 40–19 ka and is related to the straightening and narrowing of the Y channel in response to changing sediment supply [*Jobe et al.*, 2015].

Within an individual margin deposit, individual beds can be traced between cores (e.g., Figure 5). An outstanding example of this facies similarity and correlability are cores g16 and g22, located 160 m apart at the same elevation in the same margin deposit (Figures 2 and 11). The two cores show notable bed-by-bed correlability, with almost every sand-mud couplet easily identified in both cores (Figure 11). Because g16 and g22 are at the same water depth/elevation above channel thalweg (g16 at 1147.23 m and g22 at 1147.96 m), one might expect the same bed thickness in both cores. However, a comparative

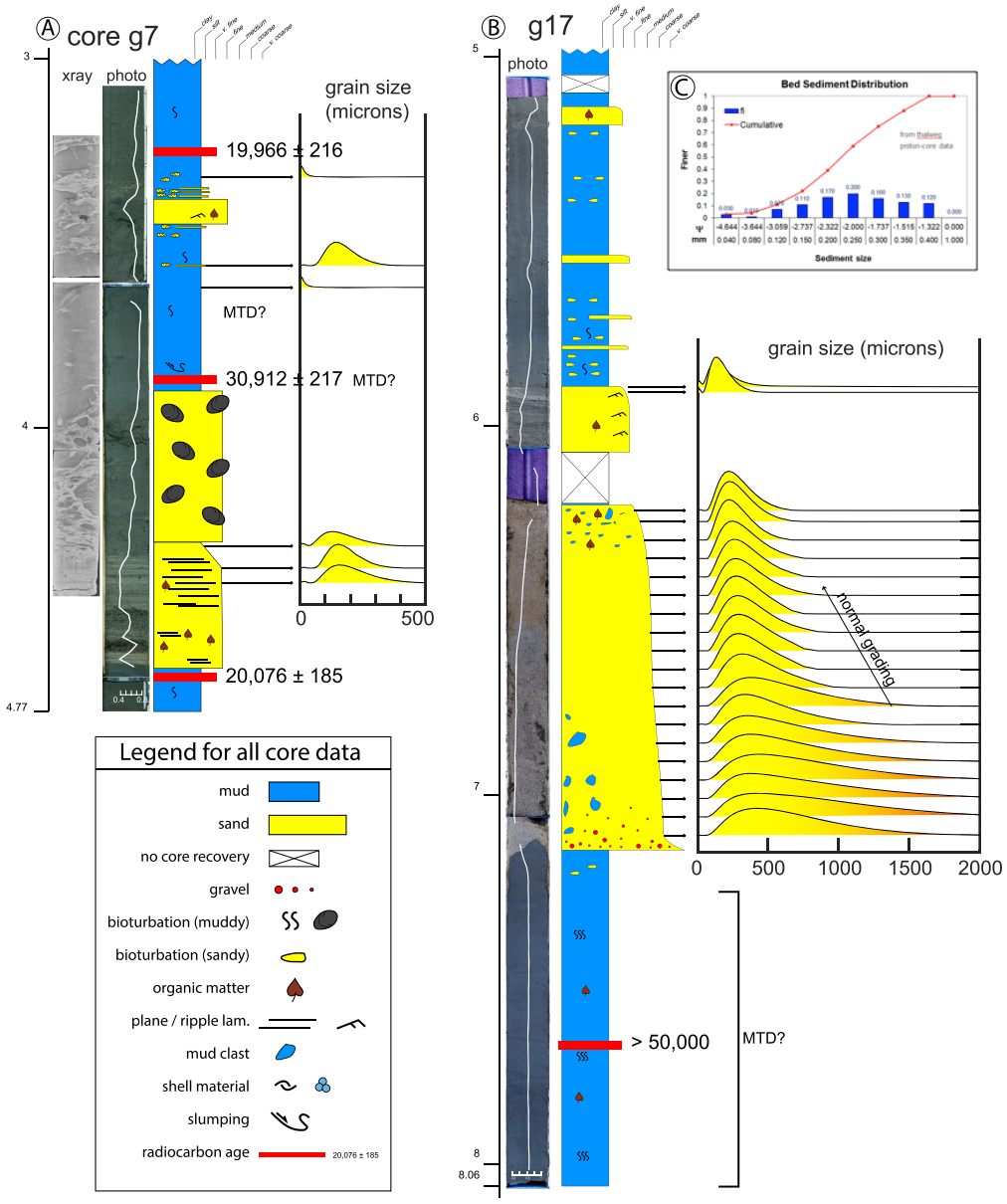

Figure 7. Axial facies of the Y channel, with core photos, core X-rays, porosity (white line on photo), visual core description, and laser grain-size distributions (muddy upper portion of cores not shown). (a) Core g7 has thick-bedded, amalgamated sands interbedded with MTDs (see out-of-sequence date at 3.8 m). (b) Core g17 has thick, normally graded sand beds with granules underlain by an MTD sourced from older sediments. See Figures 3 and 5 for core locations. (c) Combined grain-size distribution for the Y channel axis/thalweg deposits, and the nine grain-size classes used in the numerical model.

bed thickness plot demonstrates that sand beds in g16 are slightly thicker (8.5 mm, on average) than in g22 (Figure 11d). The thicker beds in g16 are likely caused by its location with respect to the Y channel thalweg. Core g16 is located at the front (updip edge) of the margin deposit where thicker sand beds were deposited, whereas g22 has slightly thinner sand beds as a result of being located at the rear of the margin deposit (Figure 2). This downstream-thinning trend is fairly consistent through the length of the core, and a thinning rate versus depth plot shows this relationship (Figure 11e). Finally, the bed-by-bed correlations are corroborated by radiocarbon dates. Deposition rates calculated for g16 (13.5 cm/ka) and g22 (22.4 cm/ka) are quite similar considering they are calculated over different depth/time intervals (Figure 11a). These observations indicate that the channel margin is a stable, aggradational environment with little modification by erosion or mass wasting processes.

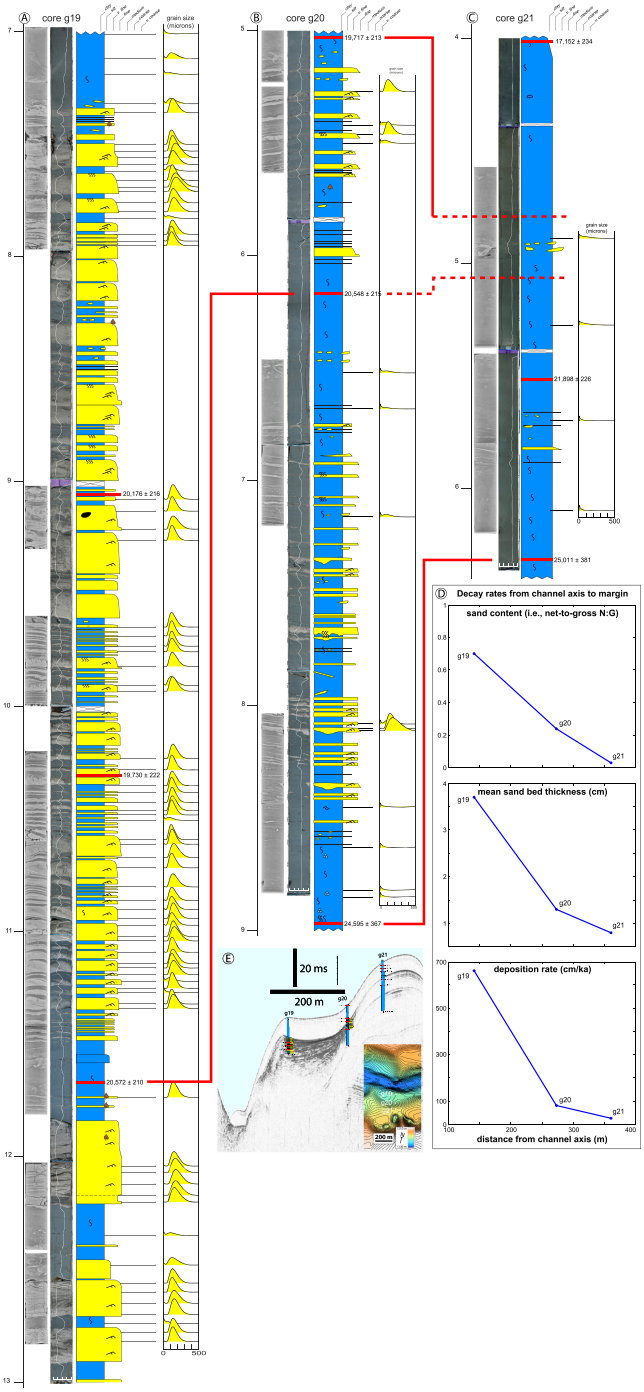

Figure 8. Margin facies of the Y channel, with cores (a) g19, (b) g20, and (c) g21. The red lines indicate age correlations, demonstrating the facies change from proximal to distal margin. (d and e) Plots showing the consistent decrease in sand content, bed thickness, and deposition rate above and away from the channel axis. See Figures 8e and 5 for core locations. Muddy upper portions of cores not shown.

3.1. Vertical Changes in Grain Size and Bed Thickness

Axis-margin facies relationships are well defined from core and chirp data in the Y channel but represent only a qualitative description of lateral and vertical facies change. These data can also be used to develop a quantitative description of grain-size and bed thickness variations as a function of the height above channel thalweg (HAT). We choose to constrain these facies changes with a vertical dimension (HAT) rather than a lateral dimension (distance from channel centerline) because it facilitates easier comparison to numerical models that characterize vertical velocity and sediment concentration profiles. However, due to the concavity of any channel cross section, an increase in HAT necessarily correlates with increasing lateral distance from thalweg (Figure 5).

Each core is assigned a "thalweg depth" by adding the Holocene mud-drape thickness to the water depth of the nearby modern channel thalweg. For example, the core transect g7-g9-g10 (Figures 5a and 9) is assigned a thalweg depth of 1315.3 m by taking the water depth at the core in the thalweg (g7 at 1312.0 m) and adding the mud drape thickness (3.3 m) measured in the core (Figure S1). The HAT value is then calculated by subtracting the elevation of each sand bed or grain-size sample from the thalweg depth assigned to that core (Table S1). Since sand beds recovered in the axis have an elevation below the assigned thalweg depth, the HAT values of these sand beds are negative (e.g., core g7), while sand beds in the margin (e.g., core g9) have positive values that decrease with increasing core depth. With this framework, the bed thickness and grain-size distributions from each core can be compared with respect to the height above thalweg (HAT). We hypothesize that cores with similar HAT should have similar bed thickness and grain-size distributions. For example, cores g16 and g22 have very similar bed thickness distributions (Figure 11) due to HAT values of 41.7 and 42.7 m, respectively.

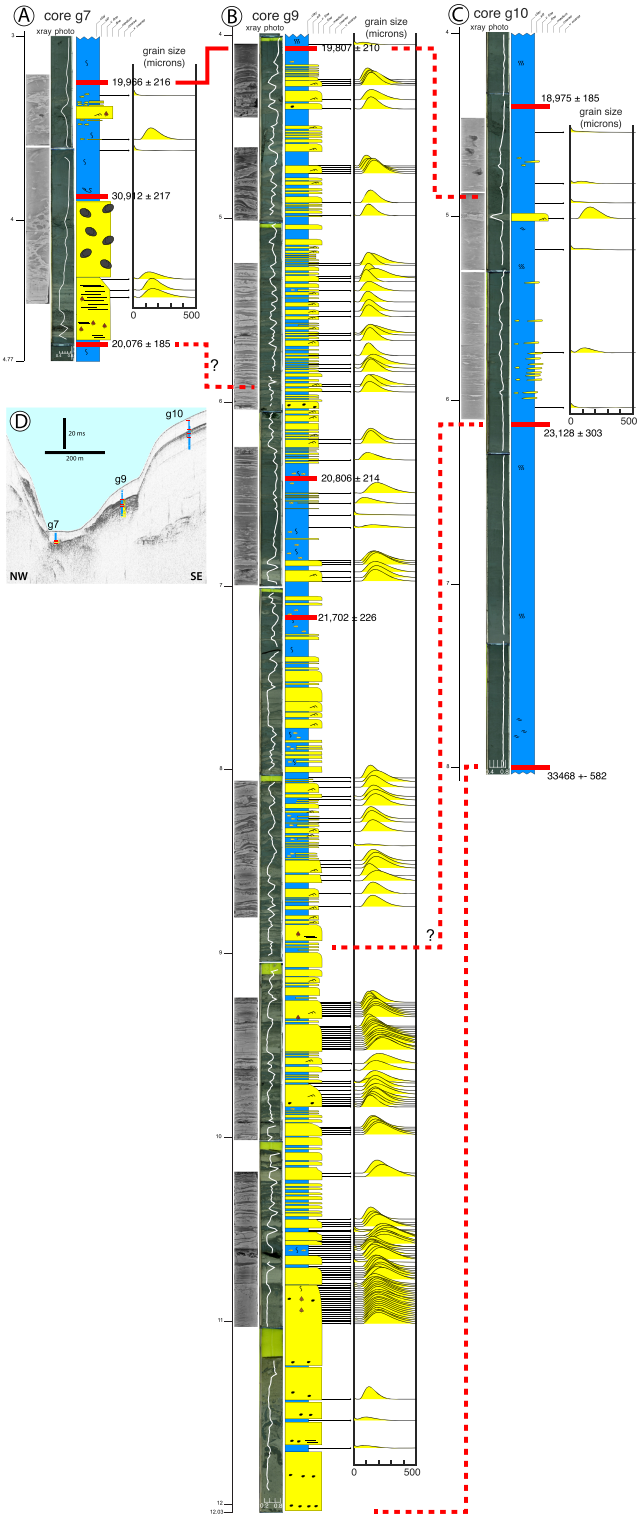

Figure 9. Axis to margin facies transition, with cores (a) g7, (b) g9, and (c) g10 (C). The red lines indicate (d) age correlations, demonstrating the drastic facies change from axis to margin. See Figures 9d and 5 for core locations. Muddy upper portions of cores not shown.

A compilation of core data reveals that bed thickness decreases strongly with increasing height above thalweg (Figure 12). Because bed thickness has a lognormal distribution [*Sylvester*, 2007], large bed thickness values best illustrate the inverse relationship with HAT (Figure 12). For example, the P_{75} (i.e., Q3) values of bed thickness are 19, 10, 3.1, 2.8, and 1.6 cm at 0, 10, 20, 30, and 40 m HAT (Figure 12). Grain-size distributions were measured in 237 sand beds by using a particle-size analyzer (histograms in Figures 7–10). All grain-size fractions (e.g., D_{10}, D_{50}, and D_{90}) show a marked decrease in grain size with increasing height above thalweg (HAT) (Figure 13). However, the coarse fraction (D_{90}) most clearly shows this relationship, with a 2 ψ unit decrease (i.e., 1 mm to 0.25 mm) from 0 m to 25 m HAT (Figure 13).

3.2. Predicting Grain-Size and Bed Thickness Trends With a Numerical Model

3.2.1. Model Description

The strong relationships between grain size, bed thickness, and height above channel thalweg (HAT) observed in the Y channel (Figures 12 and 13) can be interpreted by considering velocity and suspended sediment concentration profiles in turbidity currents. We use an existing in-channel sedimentation model developed by *Bolla Pittaluga and Imran* [2014] that is able to quantify the influence of flow properties on vertical and lateral changes in bed thickness and grain size in submarine channels. The model is a relatively simple formulation that is able to describe vertical profiles of turbidity currents flowing in a confined channel under steady and quasi-uniform flow conditions. The steady flow assumption relies on the observation that the bed evolution occurs on a time scale that is long compared to the time for unsteady passage of the flow front. This allows us to approximate the flow as steady. On the contrary, while the flow is steady on hydrodynamic

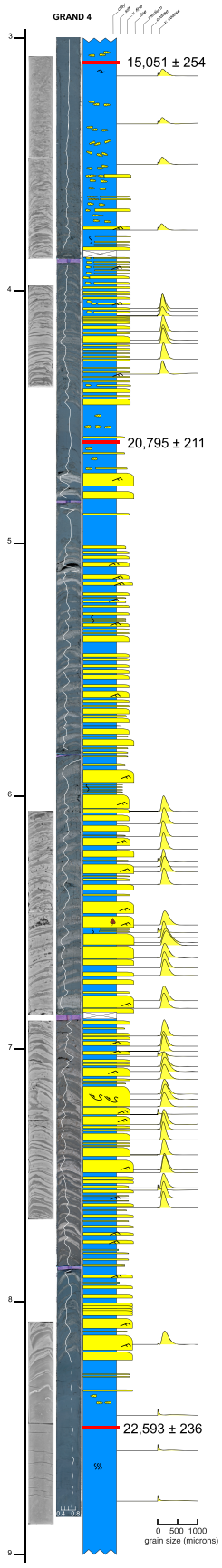

timescales, on morphologic time scales the flow evolves due to gradual changes in the underlying bed morphology, which evolves according the Exner equation.

The model assumes that currents occupy a bankfull flow condition. This is supported by the erosion of mud interbeds in the axis (Figure 7) but preservation of those mud interbeds in the margin (Figure 8), indicating that the flows were thick enough to provide sufficient shear stress to erode in the axis. The longitudinal flow and concentration profiles predicted by the model are also based on the assumption that inertial and centrifugal forces that act on a flow in a curved channel and the resulting secondary circulation [*Hay*, 1987; *Straub et al*., 2011; *Abd El-Gawad et al*., 2012] as well as overspill [*Piper and Normark*, 1983] are neglibile. While not fully realistic, these are standard simplifications widely employed in model formulations; hence, we feel that the model is appropriate to aid in the prediction of facies distribution in submarine channel environments.

The model does not explicitly solve the equations in the lateral direction. Under the assumption that suspended sediment are well mixed in the cross section, the suspended sediment concentration is considered a function of the elevation above thalweg only. As a consequence, individual depositional rates are calculated at each elevation simply by multiplying the suspended sediment concentration of each class of particle diameter to the corresponding particle settling velocity. Similarly, sediment entrainment rate is proportional to the excess of shear stress at the bed and it is estimated on the basis of the local value

Figure 10. Detail of margin facies in the g4 core. Note the gradual thinning upward profile, tied to margin aggradation (i.e., increasing distance above thalweg [cf. *Dennielou et al*., 2006]). See Figure 6 for core location. Muddy upper portion of core not shown.

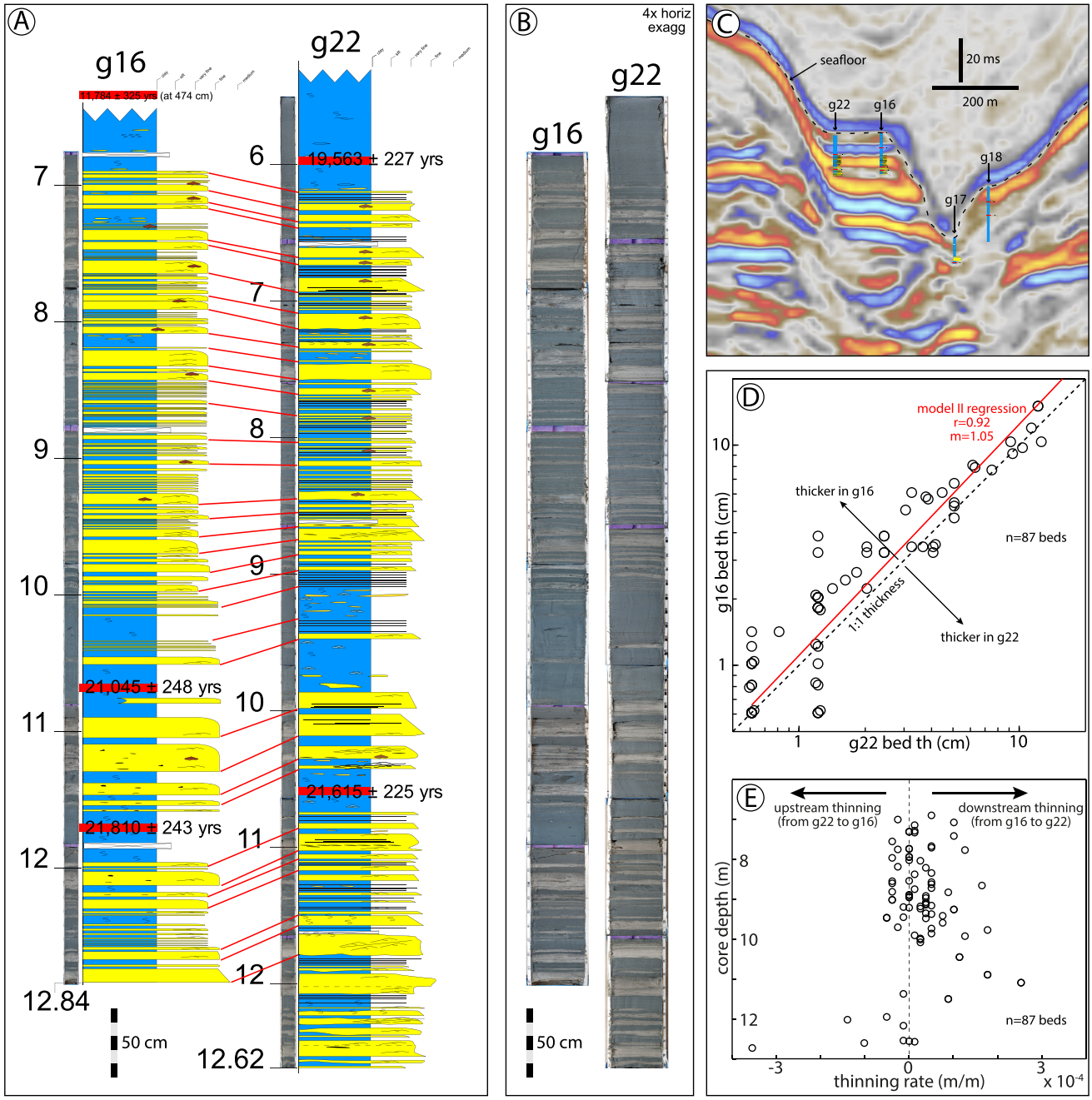

Figure 11. Correlation of cores g16 and g22, 160 m apart on the same margin deposit (see Figure 2 for location). (a) Core descriptions and sand bed correlations (red lines). Radiocarbon dates corroborate bed correlations. (b) Core photos exhibiting the remarkable correlability of nearly every sand bed between g16 and g22. (c) Arbitrary seismic reflection profile showing the location of g16 and g22 in context to other cores (see Figure 2 for location). Note that the two cores are at the same elevation. (d) Cross plot of correlated sand bed thickness, demonstrating that most sand beds are thicker in core g16. (e) Thinning rate plotted against core depth, showing that most sand beds thin downstream, from g16 to g22.

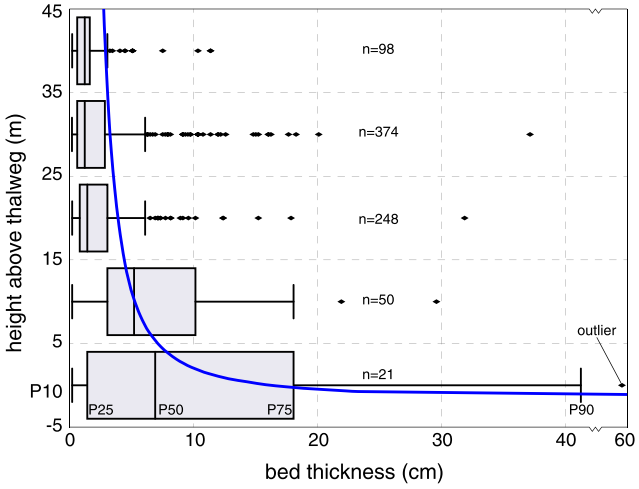

Figure 12. Box plot of bed thickness versus height above thalweg (HAT), demonstrating the decrease in bed thickness with increasing HAT. The box and whiskers show P_{10}–P_{90} values, with black dots indicating outliers. The blue line shows the result of the numerical model, which only slightly overpredicts bed thickness in the upper part of the flow.

of flow depth under the steady and uniform flow hypothesis. The model solves for deposition rate and deposit grain size at each location along the channel cross section according to the Exner equation.

Figures 14 and 15 show a sample application of the model applied to a cross section of the Niger Y channel by using only two sediment classes (mud at 40 μm and sand at 200 μm). Flow velocity and sediment concentration are predicted to vary with increasing HAT (Figure 14a), while a decrease in deposition rate and grain size with increasing HAT is shown in Figure 14b. The corresponding spatial distribution of deposition and erosion in the model (Figure 15) demonstrates preferential erosion of mud and deposition of sand in the channel axis/thalweg, and decreasing grain size with increasing HAT. It is worth noting that these spatial distributions of erosion and deposition correspond to the body of the current only and do not account for the deposition of suspended sediment associated with the tail of the current.

3.3. Comparing Model Predictions to the Y Channel Data

Inputs for the model from the Y channel data set consist of (1) *reach-averaged channel cross section* derived from bathymetry (Figure 15a); (2) *flow depth* of 80 m, inferred from the cross section; (3) *effective duration of deposition (i.e., flow duration)* of 0.1–0.2 h; (4) *bulk flow velocity* (1.2 m/s) and *depth-averaged sediment concentration* ($C = 7.7 \times 10^{-4}$), and (5) *the grain-size distribution of the Y channel axis*, which was constructed from 22 laser particle size analyses from axis cores and binned into nine grain-size classes (Figure 7c). In order to obtain the reach-averaged cross section we have first extracted 300 cross sections along the 20 km long reach investigated and then averaged the bed elevation at each lateral distance in order to get one single cross section representative of the entire reach. We have then applied the model to the averaged cross section only, characterized by a longitudinal slope equal to the average slope of the reach. Flow velocity and depth-averaged sediment concentration have been estimated by assuming a balance between friction and gravity, which is reasonable considering the approximately constant reach thalweg gradient and cross-sectional shape and area. The value of duration of deposition is calibrated to the actual bed thickness distribution from the cores of the Y channel (Figure 12). The values of flow velocity (1.2 m/s) and depth-averaged concentration ($C = 7.7 \times 10^{-4}$) obtained from the model agree fairly well with the empirical relation by *Sequeiros* [2012] that provides $U = 1.35$ m/s. The effective duration of the depositional process is smaller than the total flow duration, since it only accounts for the time required by the flow to trigger the net deposit and not for the time when the entire erosional and depositional processes do occur. This effective duration has been used as a calibration parameter to match the total thickness of the deposit observed.

With these data inputs, the model satisfactorily matches the grain-size trend with HAT (Figure 13). The model also matches the bed thickness trend with HAT (Figure 12), with only a slight overprediction of bed thickness in the upper part of the flow. This difference is probably caused by (1) our assumption of an average cross section, when in reality the bed thickness data come from inner and outer bends with different margin angles, and (2) our assumption that each flow transports the same volume of sediment. Core data from the margin (e.g., Figure 11) indicate that bed thickness is variable, suggesting a distribution of flow volumes. While out of scope for the present study, a future study could evaluate the effects on of flow volume distribution and differing margin angles. We have also explored the sensitivity of the model to different input parameters and found that the model results agree fairly well when increasing the flow velocity up to 2 m/s or varying the

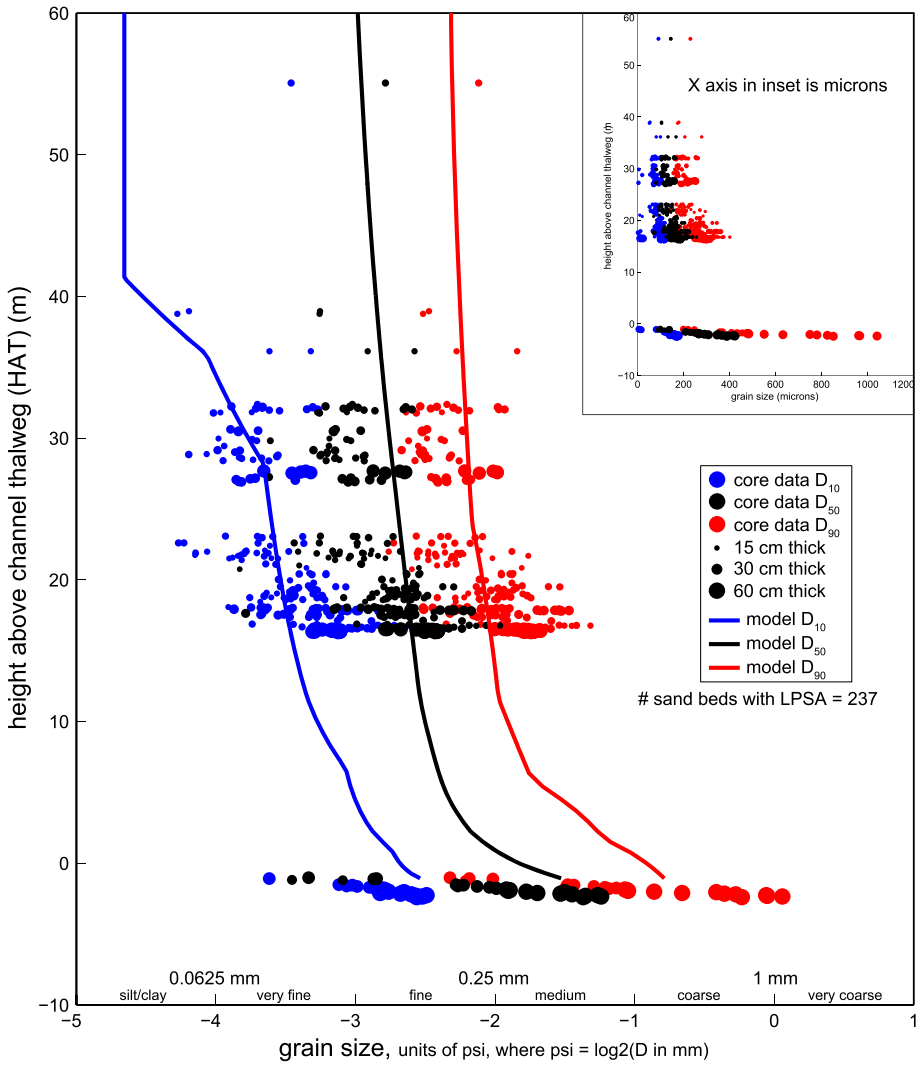

Figure 13. Plot of laser grain-size data versus height above thalweg (HAT), with dots sized by bed thickness. Note the decrease in grain size with increasing HAT (particularly the coarse D_{90} fraction in red). The solid lines are the result of the numerical model. Note the close match between the data and the model results, indicating a predictive relationship.

depth-averaged concentration ±100%. However, the model is quite sensitive to the grain-size distribution of the channel axis (Figure 7c). The effective duration of deposition provided by the model (0.1–0.2 h) is consistent with observations [*Talling et al.*, 2013] and calculations [*Jobe et al.*, 2012] from field data. The overall agreement of the model results with the data suggests that the model is robust and can be used (1) as a predictive tool and (2) to explore the parameter space for flow properties from real-world data sets.

3.4. Implications for Outcrop and Subsurface Interpretation

Our data indicate that thick, coarse-grained, amalgamated sands in the channel axis quickly transition to contemporaneous thin-bedded, nonamalgamated, fine-grained sands in the margin, consistent with observations in other modern submarine channels with core data [*Babonneau et al.*, 2010; *Paull et al.*, 2010; *Kolla et al.*, 2012] as well as outcropping, ancient submarine channel deposits [*Cronin et al.*, 2000; *Hickson and Lowe*, 2002; *Lyons*, 2004; *Jobe et al.*, 2010; *Di Celma et al.*, 2011; *Hubbard et al.*, 2014]. Furthermore, the modern geomorphology of the Y channel as well as radiocarbon dating of ancient Y channel deposits indicates that there is a significant difference in elevation between coeval axis and margin deposits. The architecture of the axis-margin transition, however, is quite variable within and between systems, and the chirp profiles in the Y channel demonstrate this streamwise heterogeneity (Figures 3–6). Sand beds from the axis do not

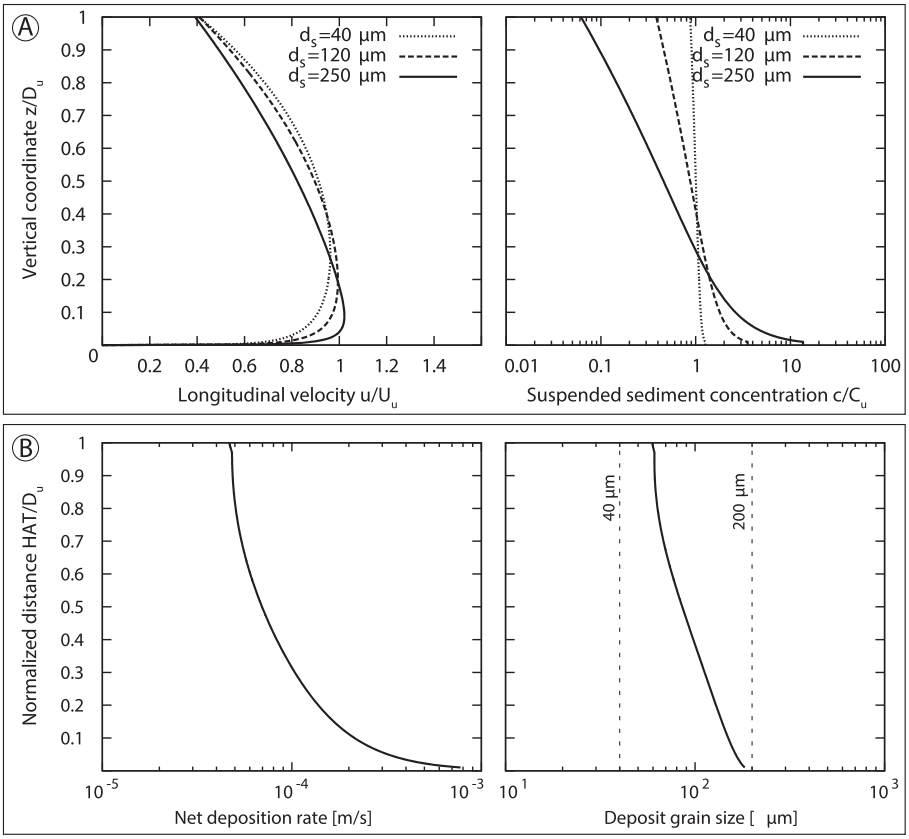

Figure 14. Sample results of the numerical model developed by *Bolla Pittaluga and Imran* [2014]. (a) Flow velocity and sediment concentration vary with increasing height above the thalweg. (b) The model predicts a decrease in deposition rate and grain size with increasing height above thalweg (HAT). Full model predictions for the Y channel are shown in Figures 12 and 13.

continue into the margin, and the two facies are separated by an erosional surface (e.g., Figure 6), suggesting that sandy channel fill seen in outcrops is younger than laterally adjacent margin deposits. Filling the modern Y channel with axis-facies sands would yield axis-margin stratal architecture similar to outcrops described by *Hubbard et al.* [2014]. The difference in the number of sand beds between the axis and margin in the Y channel indicates that many flows must have deposited thin sands in the margin while bypass/erosion occurred in the thalweg/axis [cf. *Hubbard et al.*, 2014].

Many margin/inner-levee successions show a fining and thinning upward trend that records increasing channel relief through time [*Shew et al.*, 1994; *Clemenceau*, 1995; *Manley et al.*, 1997; *Dennielou et al.*, 2006; *Migeon et al.*, 2012]. This seems to be the case for the most recent phase of the Y channel, where the margin aggrades while the axis remains in bypass, leading to increased channel relief. The thinning upward trends in cores g4, g9, g16, g16, g19, and g22 (Figure S1) record this increasing channel relief, supporting inferences of margin/inner levee growth in the Y channel [*Jobe et al.*, 2015].

We acknowledge that there can be significant differences between geomorphic channels and their preserved stratigraphic expression; therefore, the application of these results to ancient submarine channel deposits must be done cautiously. Furthermore, many submarine channel belts (including older deposits of the Y channel [see *Jobe et al.*, 2015]) show a variety of channel dimensions and architecture, and discerning these in the subsurface with limited data can be difficult. We also focus on vertical facies changes but recognize that there is abundant field data to constrain lateral facies changes in submarine channel environments [*Kane et al.*, 2007; *Kane et al.*, 2010; *Kane and Hodgson*, 2011; *Morris et al.*, 2014; *Hansen et al.*, 2015].

However, we feel that with caution, the relationships between grain size, bed thickness, and height above channel thalweg can be used predictively to estimate location of deposition relative to the base of the

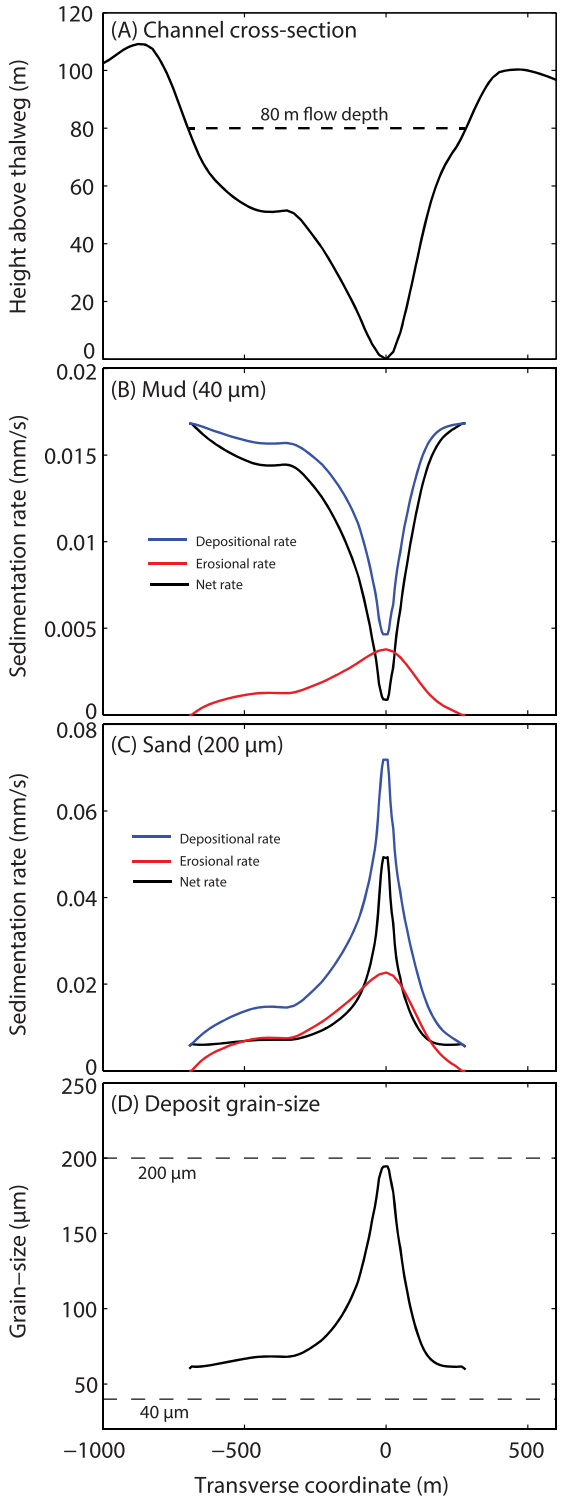

Figure 15. (a) Spatial distribution of deposition and erosion in the model calculated from a single cross section of the Niger Y channel. (b and c) The spatial rates of deposition and erosion for two grain-size classes that approximate mud and sand. (d) Deposit grain-size sedimentation and erosion, demonstrating preferential sand deposition in the axis/thalweg, and decreasing grain size with increasing HAT (compare with Figure 15a).

time-equivalent geomorphic channel when only limited data (e.g., core or outcrop) are available (Figure 16). For example, bed thickness and grain size from an unknown core may be compared with the modeled bed thickness (Figure 12) and grain-size (Figure 13) curves in order to predict channel relief and/or thalweg position (Figure 16). In the absence of core data, well logs can be interpreted in a similar manner, albeit with more uncertainty.

4. Conclusions

High-resolution seismic (chirp) and piston core data from the western Niger Delta slope demonstrate the facies architecture of the Y channel system. Thick, coarse-grained, amalgamated sands in the channel thalweg/axis transition to thin, fine-grained, bedded sands and muds in the channel margin/inner levee. An erosional surface with ~20 m relief exists between the axis and margin. Radiocarbon dates indicate that axis and margin deposits are coeval, suggesting that deposition occurs in the axis and margin by the same turbidity current, albeit with different grain sizes and facies architectures. Cores taken at the same elevation on the margin show remarkable lateral consistency of facies, indicating that the margin is a stable depositional environment with little to no erosion. Axis deposits are more heterogenous, with fast lateral facies changes and more overall heterogeneity, including occasional mass-transport-deposits.

Twenty-one piston cores from axis and margin indicate that bed thickness decreases 5 times with 20 m elevation above the channel thalweg, reflecting the axis to margin transition. Grain size (derived from a laser particle size analyzer) also decreases with height above channel thalweg, showing a 1–2 ψ decrease from axis to margin, a ~20 m elevation change. A numerical model using input data from the Y channel accurately

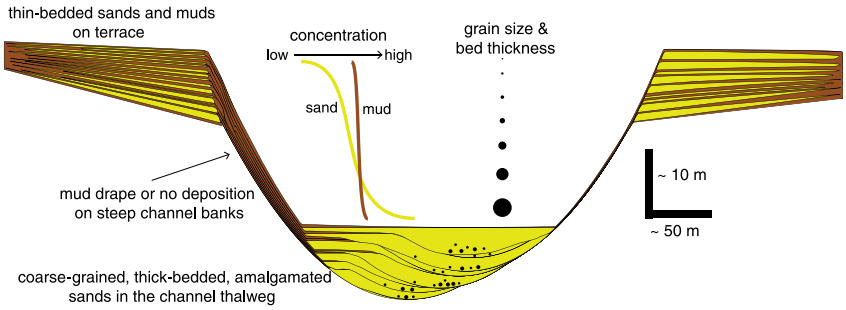

Figure 16. Conceptual diagram illustrating the vertical changes in sediment grain size and concentration in submarine channel systems that result in contrasting facies architecture between axial and marginal positions. Figure inspired by *Altinakar et al.* [1996], *Kane et al.* [2010], and *Hansen et al.* [2015].

reproduces the grain-size and bed thickness trends, suggesting that the model is widely applicable for predicting grain-size and facies architecture variations in submarine channel systems. Further work should focus on model sensitivity and applications to data-poor areas (e.g., outcrops and subsurface) to predict and better understand facies architecture in submarine channel systems.

This study emphasizes that facies models for submarine channel deposits should take into account that rapid facies change requires change in elevation above the thalweg. The transition from thick-bedded, amalgamated, coarser-grained sands in the axis to conterminous thin-bedded, nonamalgamated, finer-grained successions in the margin is primarily a reflection of a change in elevation above the channel thalweg. Even a relatively small elevation change (e.g., 1 m) is enough to result in a significant change in grain size, bed thickness, and facies architecture.

Acknowledgments

The authors would like to thank the Shell International Exploration and Production Inc. and the Shell Nigeria Exploration and Production Company for funding and permission to publish, Fugro for collection and processing of AUV data, Mary McGann and Diablo Valley Geological Services for processing core samples, Tom Guilderson at Lawrence Livermore National Laboratory for radiocarbon dating, Niall Slowey and Texas A&M University for core storage and sampling materials, and TDI-Brooks for collection of core data. Ian Kane, Octavio Sequeiros, and Anjali Fernandes provided insightful reviews that greatly improved the paper. Finally, this paper benefitted from discussions with Steve Hubbard, Brian Romans, Jake Covault, and Joris Eggenhuisen. The data used in this paper are listed in the references and supporting information. DM thanks G.Gil for continuous support and encouragement.

References

Abd El-Gawad, S. M., C. Pirmez, A. Cantelli, D. Minisini, Z. Sylvester, and J. Imran (2012), 3-D numerical simulation of turbidity currents in submarine canyons off the Niger Delta, *Mar. Geol.*, *326-328*, 55–66, doi:10.1016/j.margeo.2012.06.003.

Altinakar, M. S., W. H. Graf, and E. J. Hopfinger (1996), Flow structure in turbidity currents, *J. Hydraul. Res.*, *34*(5), 713–718, doi:10.1080/00221689609498467.

Arnott, R. W. C. (2007), Stratal architecture and origin of lateral accretion deposits (LADs) and conterminuous inner-bank levee deposits in a base-of-slope sinuous channel, lower Isaac Formation (Neoproterozoic), East-Central British Columbia, Canada, *Mar. Pet. Geol.*, *24*, 515–528, doi:10.1016/j.marpetgeo.2007.01.006.

Babonneau, N., B. Savoye, M. Cremer, and M. Bez (2010), Sedimentary architecture in meanders of a submarine channel: Detailed study of the present Congo turbidite channel (Zaiango Project), *J. Sediment. Res.*, *80*, 852–866, doi:10.2110/jsr.2010.078.

Bolla Pittaluga, M., and J. Imran (2014), A simple model for vertical profiles of velocity and suspended sediment concentration in straight and curved submarine channels, *J. Geophys. Res. Earth Surf.*, *119*, 483–503, doi:10.1002/2013JF002812.

Bouma, A. H. (1962), *Sedimentology of Some Flysch Deposits: A Graphic Approach to Facies Interpretation*, p. 168, Elsevier, Amsterdam.

Campion, K. M., A. R. G. Sprague, and M. D. Sullivan (2005), *Architecture and Lithofacies of the Capistrano Formation (Miocene-Pliocene)*, vol. 100, Pacific Section SEPM, San Clemente, Calif.

Cantero, M. I., S. Balachandar, A. Cantelli, C. Pirmez, and G. Parker (2009), Turbidity current with a roof: Direct numerical simulation of self-stratified turbulent channel flow driven by suspended sediment, *J. Geophys. Res.*, *114*, C03008, doi:10.1029/2008JC004978.

Cantero, M. I., A. Cantelli, C. Pirmez, S. Balachandar, D. Mohrig, T. A. Hickson, T.-H. Yeh, H. Naruse, and G. Parker (2011), Emplacement of massive turbidites linked to extinction of turbulence in turbidity currents, *Nat. Geosci.*, *4*, 1–4, doi:10.1038/ngeo1320.

Chapin, M., and F. Keller (2007), Channel-fill sandstones at San Clemente State Beach, California, USA. Atlas of deep-water outcrops, *AAPG Stud. Geol.*, *56*, 401–405.

Clemenceau, G. R. (1995), Ram/Powell field: Viosca Knoll 912, deepwater Gulf of Mexico, in *Turbidites and Associated Deep-Water Facies*, *SEPM Core Workshop*, vol. 20, edited by R. D. Winn and J. M. Armentrout, pp. 95–129, Society for Sedimentary Geology (SEPM) Tulsa, Okla.

Cronin, B. T., A. Hurst, H. Celik, and I. Türkmen (2000), Superb exposure of a channel, levee and overbank complex in an ancient deep-water slope environment, *Sediment. Geol.*, *132*, 205–216, doi:10.1016/S0037-0738(00)00008-7.

Dennielou, B., A. Huchon, C. Beaudouin, and S. Berné (2006), Vertical grain-size variability within a turbidite levee: Autocyclicity or allocyclicity? A case study from the Rhône neofan, Gulf of Lions, Western Mediterranean, *Mar. Geol.*, *234*, 191–213, doi:10.1016/j.margeo.2006.09.019.

Deptuck, M. E., G. S. Steffens, M. Barton, and C. Pirmez (2003), Architecture and evolution of upper fan channel-belts on the Niger Delta slope and in the Arabian Sea, *Mar. Pet. Geol.*, *20*, 649–676, doi:10.1016/j.marpetgeo.2003.01.004.

Deptuck, M. E., Z. Sylvester, C. Pirmez, and C. O'Byrne (2007), Migration–aggradation history and 3-D seismic geomorphology of submarine channels in the Pleistocene Benin-major Canyon, western Niger Delta slope, *Mar. Pet. Geol.*, *24*, 406–433, doi:10.1016/j.marpetgeo.2007.01.005.

Di Celma, C. N., R. L. Brunt, D. M. Hodgson, S. S. Flint, and J. P. Kavanagh (2011), Spatial and temporal evolution of a Permian submarine slope channel-levee system, Karoo Basin, South Africa, *J. Sediment. Res.*, *81*, 579–599, doi:10.2110/jsr.2011.49.

Dykstra, M., and B. Kneller (2009), Lateral accretion in a deep-marine channel complex: Implications for channellized flow processes in turbidity currents, *Sedimentology*, *56*, 1411–1432, doi:10.1111/j.1365-3091.2008.01040.x.

Felix, M. (2002), Flow structure of turbidity currents, *Sedimentology*, *49*, 397–419, doi:10.1046/j.1365-3091.2002.00449.x.
Felix, M., S. Sturton, and J. Peakall (2005), Combined measurements of velocity and concentration in experimental turbidity currents, *Sediment. Geol.*, *179*, 31–47, doi:10.1016/j.sedgeo.2005.04.008.
Garcia, M. H. (1990), Depositing and eroding sediment-driven flows: Turbidity currents, St. Anthony Falls Hydraulic Laboratory, Univ. of Minnesota Digital Conservancy. [Available at http://purl.umn.edu/108513.]
Hansen, L. A. S., R. H. T. Callow, I. A. Kane, F. Gamberi, M. Rovere, B. T. Cronin, and B. C. Kneller (2015), Genesis and character of thin-bedded turbidites associated with submarine channels, *Mar. Pet. Geol.*, *67*, 852–879, doi:10.1016/j.marpetgeo.2015.06.007.
Haughton, P., C. Davis, W. McCaffrey, and S. Barker (2009), Hybrid sediment gravity flow deposits—Classification, origin and significance, *Mar. Pet. Geol.*, *26*, 1900–1918, doi:10.1016/j.marpetgeo.2009.02.012.
Hay, A. E. (1987), Turbidity currents and submarine channel formation in Rupert Inlet, British Columbia: 2. The roles of continuous and surge-type flow, *J. Geophys. Res.*, *92*, 2883–2900, doi:10.1029/JC092iC03p02883.
Hickson, T. A., and D. R. Lowe (2002), Facies architecture of a submarine fan channel–levee complex: The Juniper Ridge Conglomerate, Coalinga, California, *Sedimentology*, *49*, 335–362, doi:10.1046/j.1365-3091.2002.00447.x.
Hiscott, R. N., F. R. Hall, and C. Pirmez (1997), Turbidity-current overspill from the Amazon Channel: Texture of the silt/sand load, paleoflow from anisotropy of magnetic susceptibility, and implications for flow processes, in *Proceedings of the Ocean Drilling Program*, *Sci. Results*, vol. 155, edited by R. D. Flood et al., pp. 53–78, Ocean Drilling Program, College Station, Tex.
Hosseini, S. A., A. Shamsai, and B. Ataie-Ashtiani (2006), Synchronous measurements of the velocity and concentration in low density turbidity currents using an Acoustic Doppler Velocimeter, *Flow Meas. Instrum.*, *17*, 59–68, doi:10.1016/j.flowmeasinst.2005.05.002.
Hubbard, S. M., J. A. Covault, A. Fildani, and B. W. Romans (2014), Sediment transfer and deposition in slope channels: Deciphering the record of enigmatic deep-sea processes from outcrop, *Geol. Soc. Am. Bull.*, *126*, 857–871, doi:10.1130/B30996.1.
Jobe, Z. R., A. Bernhardt, and D. R. Lowe (2010), Facies and architectural asymmetry in a conglomerate-rich submarine channel fill, Cerro Toro Formation, Sierra Del Toro, Magallanes Basin, Chile, *J. Sediment. Res.*, *80*, 1085–1108, doi:10.2110/jsr.2010.092.
Jobe, Z. R., D. R. Lowe, and W. R. Morris (2012), Climbing-ripple successions in turbidite systems: Depositional environments, sedimentation rates and accumulation times, *Sedimentology*, *59*, 867–898, doi:10.1111/j.1365-3091.2011.01283.x.
Jobe, Z. R., Z. Sylvester, A. O. Parker, N. Howes, N. Slowey, and C. Pirmez (2015), Rapid adjustment of submarine channel architecture to changes in sediment supply, *J. Sediment. Res.*, *85*, 729–753, doi:10.2110/jsr.2015.30.
Kane, I. A., and D. M. Hodgson (2011), Sedimentological criteria to differentiate submarine channel levee subenvironments: Exhumed examples from the Rosario Fm. (Upper Cretaceous) of Baja California, Mexico, and the Fort Brown Fm. (Permian), Karoo Basin, S. Africa, *Mar. Pet. Geol.*, *28*, 807–823, doi:10.1016/j.marpetgeo.2010.05.009.
Kane, I. A., B. C. Kneller, M. Dykstra, A. Kassem, and W. D. McCaffrey (2007), Anatomy of a submarine channel–levee: An example from Upper Cretaceous slope sediments, Rosario Formation, Baja California, Mexico, *Mar. Pet. Geol.*, *24*, 540–563, doi:10.1016/j.marpetgeo.2007.01.003.
Kane, I. A., W. D. McCaffrey, J. Peakall, and B. C. Kneller (2010), Submarine channel levee shape and sediment waves from physical experiments, *Sediment. Geol.*, *223*, 75–85, doi:10.1016/j.sedgeo.2009.11.001.
Khan, Z. A., and R. W. C. Arnott (2011), Stratal attributes and evolution of asymmetric inner- and outer-bend levee deposits associated with an ancient deep-water channel-levee complex within the Isaac Formation, southern Canada, *Mar. Pet. Geol.*, *28*, 824–842, doi:10.1016/j.marpetgeo.2010.07.009.
Kolla, V., A. Bandyopadhyay, P. Gupta, B. Mukherjee, and D. V. Ramana (2012), Morphology and internal structure of a recent upper Bengal fan-valley complex, in *Application of the Principles of Seismic Geomorphology to Continental-Slope and Base-of-Slope Systems: Case Studies From Seafloor and Near-Seafloor Analogues: SEPM*, *Spec. Publ.*, vol. 99, edited by B. E. Prather et al., pp. 347–369, Society for Sedimentary Geology (SEPM) Tulsa, Okla.
Lowe, D. R. (1982), Sediment gravity flows: II Depositional models with special reference to the deposits of high-density turbidity currents, *J. Sediment. Res.*, *52*, 279–297.
Lowe, D. R., and M. Guy (2000), Slurry flow deposits in the Britannia Formation (Lower Cretaceous), North Sea: A new perspective on the turbidity current and debris flow problem, *Sedimentology*, *47*, 31–70, doi:10.1046/j.1365-3091.2000.00276.x.
Lyons, W. J. (2004), Quantifying channelized submarine depositional systems from bed to basin scale, PhD thesis, p. 252, Woods Hole Oceanographic Institution and Massachusetts Institute of Technology, Woods Hole, Mass.
Manley, P. L., C. Pirmez, W. Busch, and A. Cramp (1997), Grain-size characterization of Amazon Fan deposits and comparison to seismic facies units, in *Proceedings of the Ocean Drilling Program*, *Sci. Results*, vol. 155, edited by R. D. Flood et al., pp. 35–52, Ocean Drilling Program, College Station, Tex.
McCaffrey, W. D., C. M. Choux, J. H. Baas, and P. D. W. Haughton (2003), Spatio-temporal evolution of velocity structure, concentration and grain-size stratification within experimental particulate gravity currents, *Mar. Pet. Geol.*, *20*, 851–860, doi:10.1016/j.marpetgeo.2003.02.002.
McHargue, T., M. J. Pyrcz, M. D. Sullivan, J. D. Clark, A. Fildani, B. W. Romans, J. A. Covault, M. Levy, H. W. Posamentier, and N. J. Drinkwater (2011), Architecture of turbidite channel systems on the continental slope: Patterns and predictions, *Mar. Pet. Geol.*, *28*, 728–743, doi:10.1016/j.marpetgeo.2010.07.008.
Migeon, S., T. Mulder, B. Savoye, and F. Sage (2012), Hydrodynamic processes, velocity structure and stratification in natural turbidity currents: Results inferred from field data in the Var Turbidite System, *Sediment. Geol.*, *245–246*, 48–62, doi:10.1016/j.sedgeo.2011.12.007.
Morris, E. A., Hodgson, D. M., Brunt, R. L., and Flint, S. S. (2014), Origin, evolution and anatomy of silt-prone submarine external levées, in *Sedimentology*, vol. 61, edited by P. Talling, pp. 1734–1763, doi:10.1111/sed.12114.
Parker, A. O., M. W. Schmidt, Z. R. Jobe, and N. C. Slowey (2016), A new perspective on West African hydroclimate during the last deglaciation, *Earth Planet. Sci. Lett.*, *449*, 79–88, doi:10.1016/j.epsl.2016.05.038.
Paull, C. K., W. Ussler III, D. W. Caress, E. Lundsten, J. A. Covault, K. L. Maier, J. Xu, and S. Augenstein (2010), Origins of large crescent-shaped bedforms within the axial channel of Monterey Canyon, offshore California, *Geosphere*, *6*, 755–774, doi:10.1130/GES00527.1.
Piper, D. J. W., and W. R. Normark (1983), Turbidite depositional patterns and flow characteristics, Navy Submarine Fan, California Borderland, *Sedimentology*, *30*, 681–694, doi:10.1111/j.1365-3091.1983.tb00702.x.
Pirmez, C., and J. Imran (2003), Reconstruction of turbidity currents in Amazon Channel, *Mar. Pet. Geol.*, *20*, 823–849, doi:10.1016/j.marpetgeo.2003.03.005.
Pirmez, C., R. T. Beaubouef, S. J. Friedmann, and D. C. And Mohrig (2000), Equilibrium profile and base level in submarine channels: Examples from late Pleistocene systems and implications for the architecture of deepwater reservoirs: SEPM, Gulf Coast Section 20th Annual Bob F. Perkins Research Conference, Global Deep-Water Reservoirs, p. 782–805.
Sequeiros, O. E. (2012), Estimating turbidity current conditions from channel morphology: A Froude number approach, *J. Geophys. Res.*, *117*, C04003, doi:10.1029/2011JC007201.

Sequeiros, O. E., B. Spinewine, M. H. Garcia, R. T. Beaubouef, T. Sun, and G. Parker (2009), Experiments on wedge-shaped deep sea sedimentary deposits in minibasins and/or on channel levees emplaced by turbidity currents. Part I. Documentation of the flow, *J. Sediment. Res.*, *79*, 593–607, doi:10.2110/jsr.2009.064.

Sequeiros, O. E., B. Spinewine, and R. T. Beaubouef (2010), Characteristics of velocity and excess density profiles of saline underflows and turbidity currents flowing over a mobile bed, *J. Hydraul. Eng.*, *136*, 412–433, doi:10.1061/ASCEHY.1943-7900.0000200.

Shew, R. D., D. R. Rollins, G. M. Tiller, C. J. Hackbarth, and C. D. White (1994), Characterization and modeling of thin-bedded turbidite deposits from the Gulf of Mexico using detailed subsurface and analog data, in *Submarine Fans and Turbidite Systems, Sequence Stratigraphy, Reservoir Architecture, and Production Characteristics*, *Gulf Coast Sect. Soc. Econ. Paleontol. and Min. 15th Annu. Res. Conf.*, edited by P. Weimer, A. H. Bouma, and B. F. Perkins, pp. 327–334, Society for Sedimentary Geology (SEPM), Tulsa, Okla.

Straub, K. M., and D. Mohrig (2008), Quantifying the morphology and growth of levees in aggrading submarine channels, *J. Geophys. Res.*, *113*, F03012, doi:10.1029/2007JF000896.

Straub, K. M., D. Mohrig, B. McElroy, J. Buttles, and C. Pirmez (2008), Interactions between turbidity currents and topography in aggrading sinuous submarine channels: A laboratory study, *Geol. Soc. Am. Bull.*, *120*, 368–385, doi:10.1130/B25983.1.

Straub, K. M., D. Mohrig, J. Buttles, B. McElroy, and C. Pirmez (2011), Quantifying the influence of channel sinuosity on the depositional mechanics of channelized turbidity currents: A laboratory study, *Mar. Pet. Geol.*, *28*, 744–760, doi:10.1016/j.marpetgeo.2010.05.014.

Sylvester, Z. (2007), Turbidite bed thickness distributions: Methods and pitfalls of analysis and modelling, *Sedimentology*, *54*, 847–870, doi:10.1111/j.1365-3091.2007.00863.x.

Talling, P. J., C. K. Paull, and D. J. W. Piper (2013), How are subaqueous sediment density flows triggered, what is their internal structure and how does it evolve? Direct observations from monitoring of active flows, *Earth Sci. Rev.*, *125*, 244–287, doi:10.1016/j.earscirev.2013.07.005.

Talling, P. J., et al. (2015), Key future directions for research on turbidity currents and their deposits, *J. Sediment. Res.*, *85*, 153–169, doi:10.2110/jsr.2015.03.

Tilston, M., R. W. C. Arnott, C. D. Rennie, and B. Long (2015), The influence of grain size on the velocity and sediment concentration profiles and depositional record of turbidity currents, *Geology*, *43*, 839–842, doi:10.1130/G37069.1.

Xu, J. P. (2010), Normalized velocity profiles of field-measured turbidity currents, *Geology*, *38*, 563–566, doi:10.1130/G30582.1.